



Reaction mechanism and kinetics for CO₂ reduction on nickel single atom catalysts from quantum mechanics

Md Delowar Hossain^{1,2}, Yufeng Huang², Ted H. Yu^{2,3}, William A. Goddard III ^{2✉} & Zhengtang Luo ^{1✉}

Experiments have shown that graphene-supported Ni-single atom catalysts (Ni-SACs) provide a promising strategy for the electrochemical reduction of CO₂ to CO, but the nature of the Ni sites (Ni-N₂C₂, Ni-N₃C₁, Ni-N₄) in Ni-SACs has not been determined experimentally. Here, we apply the recently developed grand canonical potential kinetics (GCP-K) formulation of quantum mechanics to predict the kinetics as a function of applied potential (*U*) to determine faradic efficiency, turn over frequency, and Tafel slope for CO and H₂ production for all three sites. We predict an onset potential (at 10 mA cm⁻²) $U_{\text{onset}} = -0.84$ V (vs. RHE) for Ni-N₂C₂ site and $U_{\text{onset}} = -0.92$ V for Ni-N₃C₁ site in agreement with experiments, and $U_{\text{onset}} = -1.03$ V for Ni-N₄. We predict that the highest current is for Ni-N₄, leading to 700 mA cm⁻² at $U = -1.12$ V. To help determine the actual sites in the experiments, we predict the XPS binding energy shift and CO vibrational frequency for each site.

¹Department of Chemical and Biological Engineering, William Mong Institute of Nano Science and Technology, and Hong Kong Branch of Chinese National Engineering Research Center for Tissue Restoration and Reconstruction, The Hong Kong University of Science and Technology, Clear Water Bay, Kowloon, Hong Kong. ²Materials and Process Simulation Center (mc 134-74), California Institute of Technology, Pasadena, CA 91125, USA. ³Department of Chemical Engineering, California State University, Long Beach, CA 90840, USA. ✉email: wag@caltech.edu; keztluo@ust.hk

Fossil fuels have been the primary source to produce energy for industrial applications and human activities for decades^{1,2}, leading to high concentration of atmospheric CO₂ that create serious environmental, ecological, and climate problems. It is now essential to find improved catalysts to convert CO₂ to useful chemicals³. Indeed progress is being made in electrochemical transformation of CO₂ into chemical fuels^{4,5}, however, the extreme stability of CO₂ makes it inert for chemical reactions in aqueous solution, demanding a large overpotential to overcome the high activation barrier. Moreover, the hydrogen evolution reaction (HER) side reaction can easily dominate under the same conditions, diminishing efficiency^{6–8}. Thus we want CO₂ reduction catalysts with high faradic efficiency for CO but negligible HER faradic efficiency. The column 11 elements (IB group) (Cu, Ag, Au) and their alloys provide the best catalysts to date^{9–14}, however, poor selectivity and stability limit their use in practical applications that which require high activity, excellent selectivity, and long-term stability. In recent years, single atom catalysts (SACs) have emerged as an effective strategy to create new electrocatalysts with maximal atomic efficiency and high selectivity for specific catalytic reactions^{15–18}. Atomically dispersed metals on suitable substrates have demonstrated unique electronic properties with great potential for electrocatalytic CO₂ reduction^{19–21}. In particular, graphene, a single atomic layer of carbon, has proved to be an effective support. It has large surface area, high conductivity, high stability, and the capability to tune electronic properties by forming strong chemical bonds to guest atoms^{22–24}. Several experimental studies have been published recently on the CO₂ reduction reaction (CO₂RR) for the nickel single atom catalysts (Ni-SACs) on graphene^{20,21,25–29}, but the performance varies markedly perhaps because of differences in the number of carbon or nitrogen bonds to Ni.

Recent developments in quantum mechanics (QM) based methods provide new tools to determine the reaction mechanisms for heterogeneous electrochemical reactions. Recently we extended the standard fixed electron QM to allow constant potential Grand Canonical QM (GC-QM) to describe the kinetics at fixed potential (U) for direct comparison to experiment³⁰. In particular, we recently developed the grand canonical potential kinetics (GCP-K) method to combine fixed charge and fixed potential QM to allow the reaction barriers to change continuously as the applied potential is changed, leading directly to current versus potential relation (Tafel slope)³¹.

Here we report the application of GCP-K to predict the reaction mechanism and rates for CO₂RR over Ni-SACs for the Ni-N₂C₂, Ni-N₃C₁, and Ni-N₄ sites in graphene. We find that Ni-N₂C₂ leads to the lowest onset potential of -0.84 V (vs RHE) to achieve 10 mA cm^{-2} current density, leading to a Tafel slope of 52 mV dec^{-1} and a turn-over frequency (TOF) of 3903 h^{-1} per Ni site at neutral (pH 7) electrolyte conditions, showing best agreement with various experimental observations at lower overpotentials. We predict the onset potential for 10 mA cm^{-2} current density of -0.92 V for Ni-N₃C₁ and -1.03 V for Ni-N₄ (which exhibits the highest saturation current for high applied potentials). We use quantum mechanics to predict the binding energy (BE) shift for the N and C 1s X-ray photoelectron spectroscopy (XPS) and the CO vibrational frequencies to help interpret the experimental nitrogen coordinations in Ni-SACs. We predict that the N 1s BE shift ranges from $+1.18$ to $+0.96$ eV for Ni-N₄ and Ni-N₂C₂ respectively. The adsorbed CO intermediate vibrations range from 1985 cm^{-1} (perpendicular) at -1.0 V on Ni-N₂C₂ site to 1942 cm^{-1} in the xz plane at -1.25 V applied potential on the Ni-N₄ site.

Results

Grand canonical potential kinetics formulation. Recently, we developed the GCP-K methodology to determine the kinetics for heterogeneous electrochemistry as a function of applied potential while allowing the transition states to evolve continuously³¹. GCP-K uses a Legendre transformation to convert from fixed charge free energy, $F(n)$, to grand canonical, $G(n; U)$, allowing the thermodynamic free energy for heterogeneous electrochemical reactions to depend on the applied potential (U). The derivation starts with the general definition of the grand canonical potential^{32–34}

$$G(n; U) = F(n) - ne(U_{\text{SHE}} - U) \quad (1)$$

where G is the grand canonical free energy, which depends on the number of electron (n), applied potential (U vs SHE), total free energy (F) as a function of n , and electronic energy ($U_{\text{SHE}} = \mu_{e,\text{SHE}}/e$) at the standard hydrogen electrode (SHE) condition. The sign of U is defined as the potential used in experiments, i.e., $U = -0.5$ V corresponds to -0.5 V vs SHE. We calculate how the number of electrons depends on the applied potential to obtain $G(n; U)$ as a thermodynamic potential. To do this, we shift the Fermi level to correspond to the applied potential by changing the electronic band occupation, varying the number of electrons in the systems (Eq. 2)^{35,36}. Finally, we obtain GCP (U) through minimizing $G(n; U)$ according to (3)^{37,38}

$$\frac{dG(n; U)}{dn} = 0 \text{ or } \mu_e = \frac{dF(n)}{dn} = e(U_{\text{SHE}} - U) \quad (2)$$

$$GCP(U) = \min G(n; U) = \min\{F(n) - ne(U_{\text{SHE}} - U)\} \quad (3)$$

Approximating $F(n)$ locally as quadratic and minimizing $G(n; U)$ leads to a quadratic form in GCP (U). This quadratic dependence is consistent with the relevant empirical forms from other studies^{39–41}. To obtain GCP (U) we fit a quadratic expansion of $F(n)$:

$$F(n) = a(n - n_0)^2 + b(n - n_0) + c \quad (4)$$

where a , b , and c are determined from QM. Minimization of (4) (Supplementary Table 1–5) leads to Eq. (5).

$$GCP(U) = -\frac{1}{4a}(b - \mu_{e,\text{SHE}} + eU)^2 + c - n_0\mu_{e,\text{SHE}} + n_0eU \quad (5)$$

These parameters can be related to the physical quantities as follows,

First, the differential capacitance, $C_{\text{diff}} = \frac{\partial n}{\partial U} = -\frac{1}{2a}$ which leads to, $a = -\frac{1}{2C_{\text{diff}}}$

Second, at the potential of zero charge, $n(U_{\text{PZC}}) = n_0$, so we obtain

$$n(U) = -\frac{1}{e} \frac{\partial GCP(U)}{\partial U} = n_0 - \frac{1}{2ae} (b - \mu_{e,\text{SHE}} + eU),$$

Thus, we can write, $b = \mu_{e,\text{SHE}} - eU_{\text{PZC}}$

Finally, $F(n = n_0) = c$, when the system is neutral, the potential of zero charge (U_{PZC}).

Putting these physical quantities into Eqs. (4) and (5), we write the grand canonical potential and free energy expressions (Supplementary Notes 1) as in Eqs. (6) and (7)

$$F(n) = -\frac{1}{2C_{\text{diff}}}(n - n_0)^2 + (\mu_{e,\text{SHE}} - eU_{\text{PZC}})(n - n_0) + F_0 \quad (6)$$

$$GCP(U) = \frac{e^2 C_{\text{diff}}}{2} (U - U_{\text{PZC}})^2 + n_0 eU + F_0 - n_0 \mu_{e,\text{SHE}} \quad (7)$$

where, n_0 is the number of electrons at zero net charge (total number of valence electron), $\mu_{e,\text{SHE}}$ is the chemical potential of an electron vs standard hydrogen electrode (SHE), and e is the energy in eV. This quadratic form of free energy $F(n)$ and grand canonical potential GCP (U) accounts for the change in capacitance as the potential changes.

Our procedure is first to carry out QM for a range of fixed charges using VASPsol solvation. Then we use the CANDLE solvation model implemented in jDFTx to obtain the free energies at the same constant charge. Then we recalculate the constant potential free energies using the Legendre transform. For stable intermediates the optimized geometry from VASPsol is used. For transition states we use the above procedure for each point along the climbing image nudged elastic band (CI-NEB) surface so that the transition state adjusts properly as the potential is changed.

Structural model of Ni-SACs for CO₂ reduction reaction.

Experimental studies show that adding a Ni²⁺ containing metal solution to N-doped graphene oxide solution and then annealing at high temperature leads to electrocatalysts with Ni-nitrogen/carbon moieties embedded within the graphene matrix. The central Ni atom is coordinated to nitrogen/carbon(s) through strong covalent bonding, making this a single atom catalyst embedded within the graphene matrix. Each Ni may be bonded to 2 to 4 N's atom along with 2–0 C's, which we denote as Ni–N₂C₂, Ni–N₃C₁, or Ni–N₄ (refs. 16,27,42). Our calculated formation energies show that Ni–N₄ is energetically most favorable (–1.13 eV) while Ni–N₂C₂ structure (1.04 eV) is the least favorable. We examine here CO₂RR considering all three possible structures and compare their catalytic performance.

The reduction process of CO₂ into CO involves two major steps, each involving a net transfer of one electron as the reactant is transformed to product (Fig. 1). We consider all three cases of Ni–N_{4–x}C_x ($x=0–2$) as possible configurations of Ni-SAC, embedded in a 4 × 4 periodic super cell of graphene, as shown in Fig. 1a, b. We examined the Eley-Rideal (ER) mechanism⁴³ for CO₂ reduction, where water from solution reacts with an adsorbed CO₂ molecule to form *COOH and OH[–] in solution. We start with one CO₂ physisorbed on the single Ni sites including three explicit water molecules plus implicit solvation of this entire surface (Fig. 1c). As we apply a negative potential, the system builds up negative charge at the surface that induces linear CO₂ to bend slightly on Ni-SAC. This bent CO₂ facilitates a proton transfer from water to form the COOH intermediate, which binds strongly to the central Ni atom with Ni–C = 1.98–1.94 Å for various surface charges of 0–1.5 (a positive value represents excess electron compared to neutral, $n - n_0$). This proton comes from a neighboring explicit water to form either cis-COOH (with the H pointing up) or trans-COOH (with the H pointing down). Simultaneously, product OH[–] forms, stabilized by two other explicit water molecules (optimized) plus the implicit solvation, as shown in Fig. 1d, e respectively.

Figure 1f–i shows the second step of dehydroxylating the adsorbed COOH species by an explicit water to produce CO product plus H₂O and OH[–] (stabilized by water molecules and implicit solvent). The CO affinity on these Ni-SAC sites depends on the number of N's bonded to the Ni, but none have a strong affinity for CO species (unlike Ni metal catalysts)^{44,45}. Our calculations show that Ni–N₄ has the least affinity for CO (Ni–CO bond distance ~2.53–2.27 Å), leading to tilted adsorbed CO ($\angle\text{OCNi} = 116^\circ$) (Fig. 1h) while Ni–N₂C₂ sites (Fig. 1i) show relatively stronger affinity toward CO (Ni–CO distance from 1.80 to 1.92 Å) and CO adsorbed almost linearly. This adsorbed CO desorbs from the Ni site along a straight pathway ($\angle\text{OCNi} = 176.5^\circ$) to slightly tilted ($\angle\text{OCNi} = 152^\circ$) depending

on the applied potentials. The Ni–N₃C₁ site shows adsorption intermediate between Ni–N₂C₂ and Ni–N₄ sites (Supplementary Data 1).

The quadratic behavior of the grand canonical potential was examined thoroughly for the whole process. The dependence for the trans-COOH reaction on applied potential is shown in Fig. 2. Figure 2a shows that the free energy, $F(n)$ obtained from the CANDLE implicit solvation method, correlates linearly with system charge. However, subtracting the free energy contribution of each electron at SHE leads to the quadratic dependence shown in Fig. 2b, according to Eq. (6) leading to Eq. (8),

$$F(n) - \mu_{e,\text{SHE}}n = -\frac{1}{2C_{\text{diff}}}(n - n_0)^2 - \mu_{e,\text{SHE}}n_0 - eU_{\text{PZC}}(n - n_0) + F_0 \quad (8)$$

Figure 2b shows that the optimum charge is slightly negative. Thus, at zero potential, the intermediate has a little more extra charge than the neutral. In electrochemical conditions, applying a negative potential, U , shifts the free energy minimum of $G(n, U)$ by neU in Eq. (8). Figure 2c shows that this shifts the minimum of $G(n, U)$ toward higher charge (the case of $U = -0.8$ V is shown Fig. 2c), which drives the reaction toward the product containing more charge.

Transition states change as a function of applied potential.

We first carried out constant charge DFT and then transformed the free energies to obtain GCP (U), leading to transition states (TS) exactly equivalent with the results from constant potential calculations (as shown in our earlier work using the minimax theorem)^{31,46}. The free energy of the transition state, $F_{\text{TS}}(n)$ obtained from the fixed charge (n) calculation is transformed into the grand canonical potential GCP_{TS, n} (U) via a Legendre transformation. Since the transition state is the highest barrier along the minimum energy path (MEP), the TS geometry changes with applied potential, U .

Figure 3 shows how the CO₂ to OCOH reaction barrier depends on the applied potential for the three types of Ni sites along the minimum energy path and transition states at $U = -0.8$ V vs RHE. The conversion of linear CO₂ through bent CO₂ to COOH is endothermic. The slightly bent state (image 02) is followed by the transfer of a H from HOH to form OCOH plus an OH[–] stabilized by the two H₂O (images 03–04). The transition state (image 04) has a geometry similar to the *COOH intermediate but with a slightly higher energy (1.65 kcal mol^{–1}) arising from reorientation of the bottom water molecule (Fig. 3a). This protonation step has an energy barrier shown in Fig. 3b. For Ni–N₂C₂, the linear CO₂ (initial state) ($\angle\text{OCO} = 178.34^\circ$), first becomes slightly bent ($\angle\text{OCO} = 167^\circ$) at the 02 image leading to a low energy barrier (1.55 kcal mol^{–1} at $U = -0.8$ V), indicating fast decoupled electron transfer followed by proton transfer with higher energy barrier (9.24 kcal mol^{–1}) at image 04. For Ni–N₃C₁, we find a 1.97 kcal mol^{–1} energy barrier to form slightly bent CO₂ and a barrier of 17.72 kcal mol^{–1} to form OCOH. Finally, for Ni–N₄ we find a 2.31 kcal mol^{–1} energy barrier to form slightly bent CO₂ and a barrier of 26.97 kcal mol^{–1} to form OCOH at -0.8 V potential. The reaction pathways and energies for the conversion of linear CO₂ to trans-COOH are shown in Supplementary Fig. 3. In contrast to step 1, the reaction pathway for conversion of cis-COOH to CO clearly involves a sharp TS and lower energy barrier at constant applied potential as shown in Fig. 4a, b. The reaction pathway shows the bond breaking between OC–OH step (image 3) has the highest energy barrier. Among all studied sites, Ni–N₃C₁ shows the highest barrier of 10.01 kcal mol^{–1} while Ni–N₄ shows the lowest barrier of

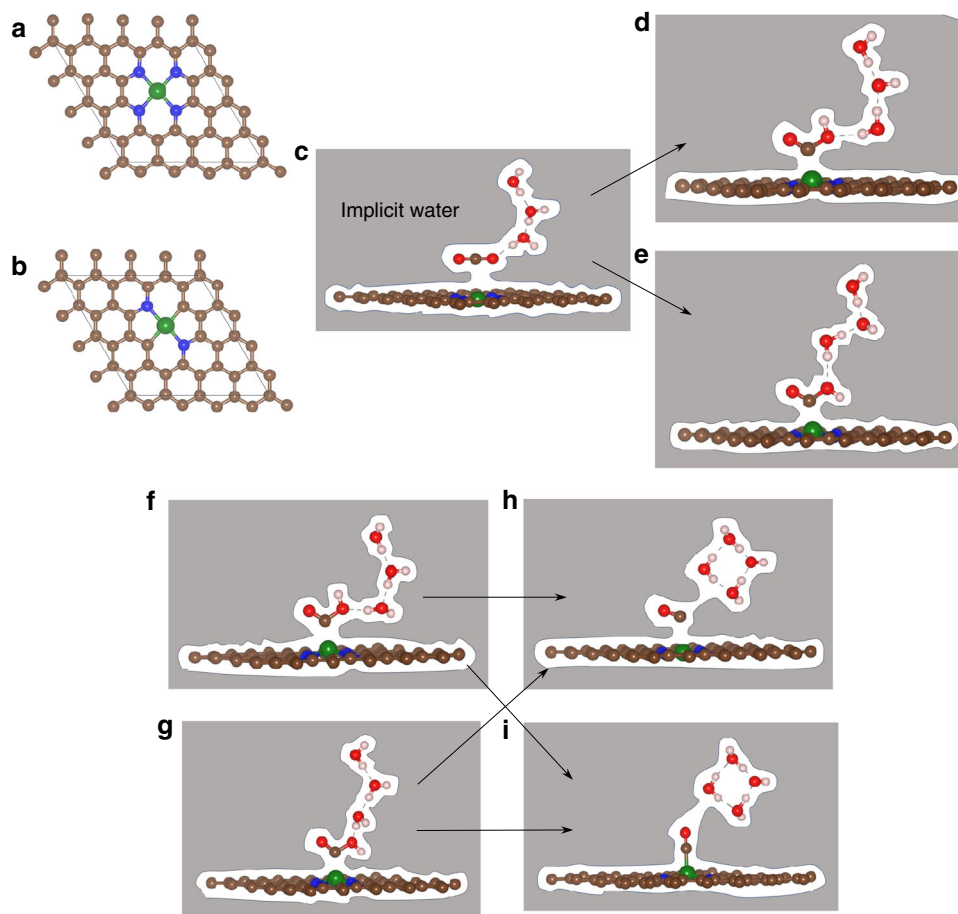


Fig. 1 The CO₂ to CO conversion process on graphene-supported nickel single site. **a, b** In all, 4 × 4 periodic Ni-SAC system containing Ni-N₄ and Ni-N₂C₂ moieties as active sites for CO reduction reaction. **c** The optimized structure of physically adsorbed CO₂ on Ni single site, is stabilized by three molecules of explicit water from solution. **d, e** The optimized structure of chemically adsorbed cis-COOH (H up) or trans-COOH (H down) respectively. The arrow sign represents the reaction direction where physically adsorbed CO₂ molecule reacts with a neighboring water molecule to produce cis- or trans-COOH intermediates together with hydroxyl ion. The later is stabilized by two explicit water molecules in the solution. **f, g** Optimized adsorbed cis- and trans-COOH intermediates on Ni-SAC respectively. **h, i** Optimized structures of CO product binding on Ni-N₄ and Ni-N₂C₂ site respectively. The arrow sign represents the reaction direction of chemisorbed COOH with water and produce CO and hydroxyl ion in solution. The CO binds on the Ni-N₂C₂ site perpendicularly representing a stronger attraction than on the Ni-N₄ site. The whole calculation was done by using implicit solvation as in VASPsol and CANDLE solvation as implemented in the VASP and jDFTx code, respectively together with three explicit H₂O to better describe the charge transfer and polarization. Supplementary Figs. 1 and 2 show that adding additional explicit waters leads to similar results, and supplementary Table 6 shows that reoptimizing the structures with jDFTx leads to negligible changes compared to the optimum structures in VASP. (Gray color to entire surface represents implicit solvation, brown: carbon, blue: nitrogen, green: nickel, red: oxygen, off white: hydrogen atom).

7.02 kcal mol⁻¹ at $U = -0.53$ V applied potential (Fig. 4b). The pathways with free energy for the formation of CO from trans-OCOH is shown in Supplementary Fig. 4.

Figure 4c–e illustrates the geometric change of the TS as a function of applied potential along the reaction path. Along the reaction path (Fig. 4a), we show two spatial coordinates: (1) distance between OC–OH in the COOH TS, which changes from 1.46 Å to 2.77 Å as $U = -0.8$ changes to 0 V (Fig. 4d) and (2) the distance between the new OH bond to the OH of COOH and the old OH bond of the H₂O molecule donating the proton changes from 1.71 Å to 1.04 Å as $U = -0.8$ V changes to 0 V (Fig. 4e).

Our results show that the TS at zero applied potential is very similar to the product but as U becomes more negative, the TS moves toward the reactant, becoming similar to the reactant at $U = -0.8$ V (Fig. 4c). As the potential becomes more negative, the reaction barrier decreases making the path more favorable to convert reactants into products. Thus, we find the OC–OH distance decrease uniformly with U (Fig. 4d) and the COOH–H₂O distance increases uniformly (Fig. 4e). The charges

associated with the adsorbed species change linearly with U , leading to a smooth reaction pathway along the reaction coordinate. At zero potential, the transformation begins with a charge of 0.4 on the Ni-SACs, which increases to 1.0 as the applied potential is increased to -0.8 V. To show the linear relationship between applied potential and charges on the species more quantitatively, we compare this reaction path for the GCP-K model with the conventional Butler–Volmer PCET kinetics in Fig. 5. This shows that at potential U_0 , the transition state, TS₀ (Fig. 5a) corresponds to the spatial geometry R₀ but as the applied potential changes to U_1 the transition state (TS₁) moves leftward toward reactant reaching to R₁ (refs. 47,48). In this grand canonical potential kinetics (GCP-K) description, the fractional charges change continuously along the reaction coordinates as the applied potential is changed, as shown in Fig. 5b, c. Initially, at zero voltage the reaction barrier is 16.89 kcal mol⁻¹, the TS has a slightly negative charge (0.4 e) and the OC–OH distance is about 2.77 Å, very similar to the product (Fig. 4c). But as the applied potential is changed to -0.8 V, the barrier decreases continuously

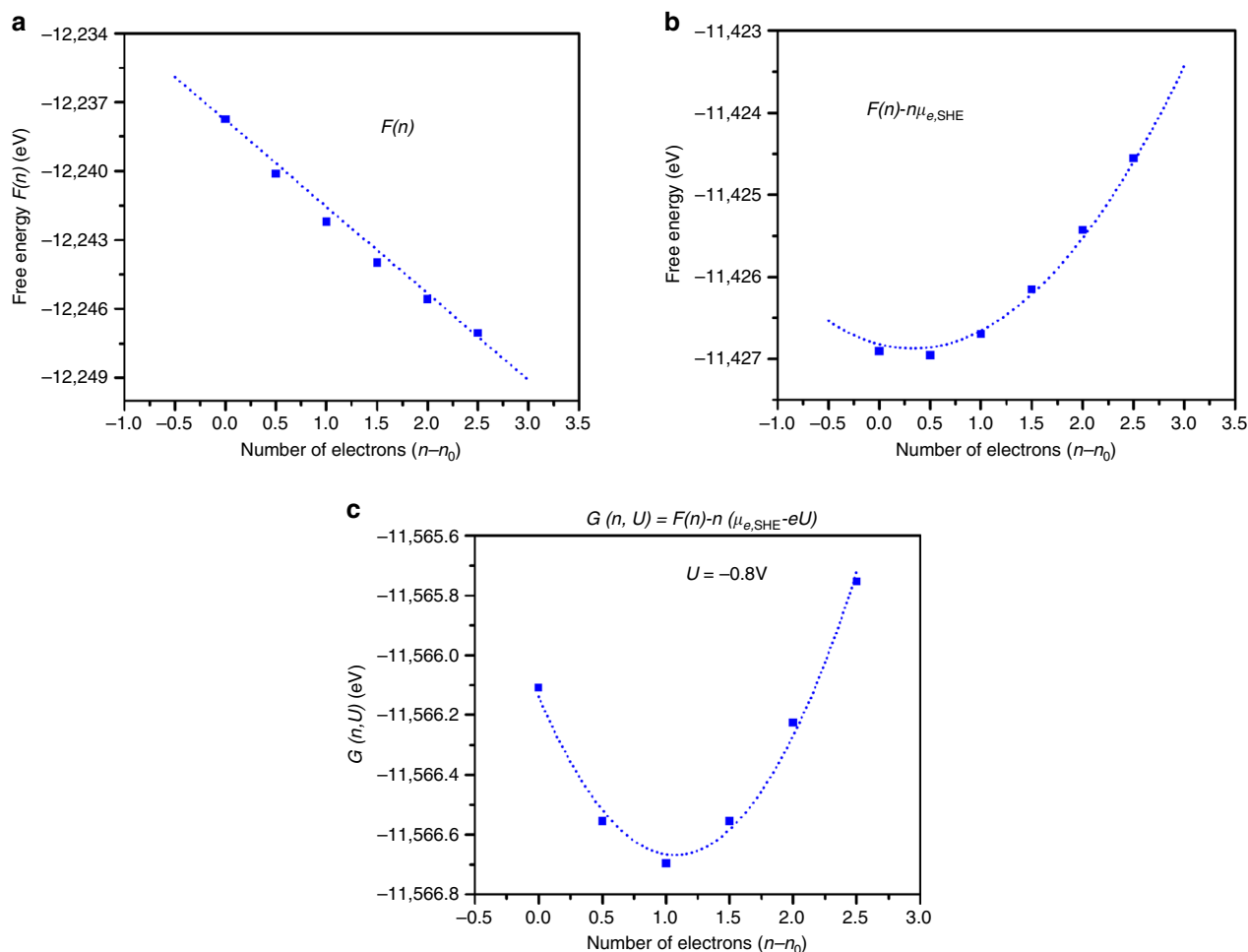


Fig. 2 Behavior of free energy and grand canonical potential as a function of the number of electrons. **a** The free energies as a function of number of electrons show a nearly linear relationship. **b** The relation between free energy and number of electrons becomes quadratic when the energy contribution of each electron at SHE are subtracted from total free energy. The quadratic dependence allows the optimum number of electrons within the system. **c** Minimization of free energy as a function of number of electron when an external potential is applied to the system. The free energy minimum is shifted toward higher electron numbers when voltage applied, ensuring that the reaction progresses in the forward direction. The blue dots represent DFT energies while the dash curve refers polynomial 2nd order fitting. Our calculated rates use cubic splines to fit the points.

to $2.98 \text{ kcal mol}^{-1}$ while the TS shifts continuously toward the reactant with a short (1.46 \AA) OC–OH distance at a more negative charge of $1.0e$. The charge difference between the transition states at 0 V ($\text{TS}_{0\text{V}}$) and -0.8 V ($\text{TS}_{-0.8}$) is $0.6e$ as shown in Fig. 5d, e. Thus, we describe the charge transfer as a potential dependent continuous process during the electrochemical reaction as the intermediates adsorb on the electrode surface and react along the reaction path leading to a smooth path for the reaction. Similarly, we observe a continuous change of the transition state (TS) with applied potential for the trans-COOH to CO conversion reaction for the Ni– N_4 site (Supplementary Fig. 5). We also observe similar behavior for the reaction at the Ni– N_2C_2 and Ni– N_3C_1 sites. As shown above, the conversion of CO_2 to COOH leads to a lower energy barrier for Ni– N_2C_2 and Ni– N_3C_1 sites than for Ni– N_4 . This makes the 2nd step reaction slightly less favorable for Ni– N_2C_2 and Ni– N_3C_1 sites. The conversion of cis-COOH and trans-COOH into CO on Ni– N_3C_1 and Ni– N_2C_2 involve higher energy barriers than on Ni– N_4 (Supplementary Figs. 6–8).

The hydrogen evolution reaction on Ni-SACs. The hydrogen evolution reaction (HER) competes with the CO_2RR , decreasing

the faradic efficiency (FE) for CO evolution. HER can take place either by reducing protons ($2\text{H}^+ + 2e^- \rightarrow \text{H}_2$) or by reduction of water ($2\text{H}_2\text{O} + 2e^- \rightarrow \text{H}_2 + 2\text{OH}^-$) from aqueous solution via the Volmer-Tafel/Heyrovsky reaction. Thus, we must examine the comparative activity of HER and CO_2RR on the same catalysts and electrolyte conditions. Since our electrolytic environment is neutral ($\text{pH } 7$), we considered the HER via water reduction. Therefore, there are two steps: In step 1 shows hydrogen from solvent water gradually moves toward Ni surface and finally adsorbs onto the Ni site via the Volmer reaction, producing OH^- solvated by the explicit H_2O molecules (Fig. 6a) and step 2 involves the adsorbed hydrogen slowly combining with a second hydrogen from solution H_2O to finally evolves as H_2 gas via the Heyrovsky reaction (Fig. 6c). Figure 6b, d show that HER depends strongly on the number of N bonded to the Ni. Thus, at $\text{pH } 7$ and $U = -0.8 \text{ V}$ applied potential we find that the hydrogen adsorption on Ni– N_2C_2 site from solvent water involves a transition state (TS) with an energy barrier of $11.43 \text{ kcal mol}^{-1}$ (Fig. 6b), while it requires relatively higher energy of $15.46 \text{ kcal mol}^{-1}$ to combine with a second hydrogen from water in solution to evolves as H_2 gas via Heyrovsky step (Fig. 6d). On the other hand, the calculated reaction barrier for the Volmer step to put

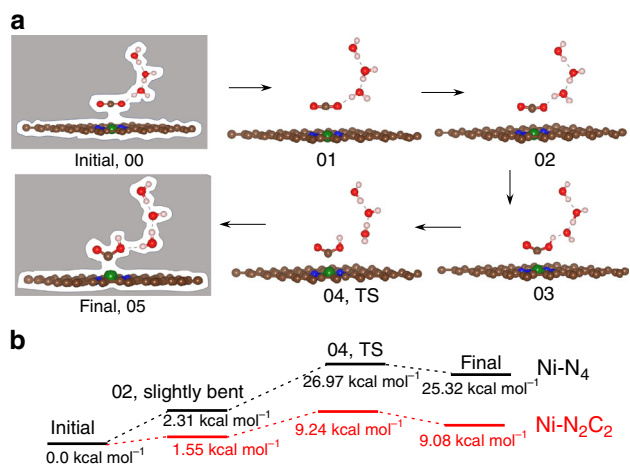


Fig. 3 Reaction pathways and barriers for CO₂ to cis-COOH conversion. **a**

The minimum energy path calculation using the CI-NEB method with implicit solvation. We consider total six images (00–05) for this process. The initial linear CO₂ interacts with neighboring water molecule to form a slightly bent structure (image 02). Later this bent CO₂ takes a proton from water to produce cis-COOH product (05 image) via the transition state (TS) at image 04. The arrow shows the forward reaction. **b** Reaction energies and TS barrier for the protonation step for CO₂ reduction on the Ni-N₄ and Ni-N₂C₂ sites at -0.8 V vs RHE applied potential. The proton transfer occurs most easily on Ni-N₂C₂, followed by Ni-N₃C₁ and Ni-N₄ site. Note that in these calculations the charge of the system changes continuously as the H moves from water to OCO to form OCOH⁺ and OH⁻. There is not a separate electron transfer step as in the proton coupled electron transfer (PCET) surface hopping picture. (Gray color: entire surface represents implicit solvation along the whole reaction pathways, brown: carbon, blue: nitrogen, green: nickel, red: oxygen, off white: hydrogen atom).

H^{*} on the surface is 15.04 kcal mol⁻¹ and the Heyrovsky step of forming H₂, it is 9.36 kcal mol⁻¹ on Ni-N₃C₁ sites. Here the H^{*} is adsorbed on the bridge sites of the Ni-C bond (Supplementary Figs. 9–10). The bond distances of C-H and Ni-H in the bridge site position are about 1.14 and 1.80 Å, respectively. The Ni-N₄ sites are least favorable for HER. The calculated reaction barrier for the Volmer step is 30.26 kcal mol⁻¹, while the Heyrovsky step has a barrier of 6.69 kcal mol⁻¹ at pH 7 and applied potential -0.8 V conditions (Supplementary Figs. 9–12). The Ni-N₄ sites are preferred to minimize HER.

Reaction mechanism for CO₂ reduction. We calculated the CO₂ reduction reaction at neutral pH condition on Ni-SACs with three different Ni sites configurations: Ni-N₂C₂, Ni-N₃C₁, and Ni-N₄ embedded in graphene. The reference fermi energy of the electron is shifted by $\text{pH} \times 0.059$ eV to put the applied potential in terms of RHE. We summarize the free energy activation barriers and reaction free energies in Fig. 7a obtained using grand canonical potential GCP (U) kinetics for all possible intermediates, transition states, and products during CO₂ reduction at pH 7 and -0.8 V vs RHE applied potential.

Overall, CO₂ reduction on Ni-N₂C₂ site via the cis pathway is most favorable at $U = -0.84$ V, the onset potential for 10 mA cm⁻² current density. But in the last step of forming CO, the bond to Ni is too strong, limiting the maximum current at more negative potentials. The CO₂ conversion to cis-COOH reaction is energetically most favorable on Ni-N₂C₂ sites. In the first step the applied potential adds negative charge to CO₂, causing it to bend. Next it reacts with a proton from a solution H₂O to form

cis-COOH via TS01 with a barrier of 9.24 kcal mol⁻¹. This cis-COOH can convert back into CO₂ with a small barrier (TS10) of 0.16 kcal mol⁻¹ or it can abstract a second hydrogen from solution to form CO plus H₂O and OH⁻ with a barrier (TS13) of 6.29 kcal mol⁻¹. This CO is strongly adsorbed on the central Ni surface; to evolve as CO gas requires a barrier (TS30) of 16.57 kcal mol⁻¹. This desorption frees up the binding site for further reaction or it can form cis-COOH again by the back reaction with a barrier (TS31) of 7.58 kcal mol⁻¹. On the other hand, linear CO₂ is converted into trans-COOH on Ni-N₂C₂ sites with a barrier (TS02) of 9.96 kcal mol⁻¹, slightly higher than cis although the reverse process has a same barrier (TS20) of 0.16 kcal mol⁻¹ or it can react with another hydrogen from solution to form adsorbed CO with slightly lower barrier (TS23) of 5.82 kcal mol⁻¹. This adsorbed CO is finally evolved into solution as CO gas with the same barrier (TS30) as cis, 16.57 kcal mol⁻¹, leaving an empty catalyst surface or it can convert into trans-COOH by back reaction with high barrier (TS32) of 7.58 kcal mol⁻¹.

Although Ni-N₂C₂ sites initiate the CO production at the lowest U , Ni-N₃C₁ dominates in the potential range of $U = -0.92$ V to -1.12 V, where the maximum current is limited due to strong bonding of CO to the Ni site. The conversion of CO₂ to cis-COOH on the Ni-N₃C₁ site leads to a barrier (TS01) of 17.72 kcal mol⁻¹, which is more uphill than Ni-N₂C₂ site. This reaction can be reversed with a very small barrier (TS10) of 0.90 kcal mol⁻¹ or it can abstract a second hydrogen from solution and convert into CO with a forward barrier (TS13) of 6.65 kcal mol⁻¹. This adsorbed CO has intermediate affinity on Ni and can evolve as CO gas with a barrier (TS30) of 10.18 kcal mol⁻¹, leaving the Ni site vacant for further reactions or it can form cis-COOH again by the reverse reaction with a barrier (TS31) of 13.46 kcal mol⁻¹. The conversion involving the trans-COOH intermediate on Ni-N₃C₁ sites is slightly easier than for the cis form. Here, the CO₂ is converted into trans-COOH with a barrier (TS02) of 14.62 kcal mol⁻¹, the reverse reaction to produce CO₂ has a small barrier (TS20) of 1.49 kcal mol⁻¹ or it can react with another hydrogen from solution to form adsorbed CO plus H₂O and OH⁻ with a relatively higher barrier (TS23) of 7.88 kcal mol⁻¹ than for cis case. The adsorbed CO can evolve as CO gas with a barrier (TS30) of 10.18 kcal mol⁻¹, leaving the active site available for next reaction or it can convert into the trans-COOH by the reverse reaction with a high barrier (TS32) of 14.67 kcal mol⁻¹.

Ni-N₄ sites produce the maximum current for CO production with higher faradic efficiency, but at higher potentials. The trans pathway provides a lower energy barrier than cis for both steps of CO production. The CO₂ conversion to cis-COOH (Supplementary Note 2) is energetically uphill by 26.97 kcal mol⁻¹ via the TS01 step on Ni-N₄ site, much higher than the other Ni sites. The cis-COOH can convert back into CO₂ with a barrier (TS10) of 1.65 kcal mol⁻¹ or it can abstract a second hydrogen from solution to form adsorbed CO at a barrier (TS13) of 2.98 kcal mol⁻¹. This CO is very weakly adsorbed on the Ni site and evolves as CO gas with a barrier (TS30) of 6.39 kcal mol⁻¹, leaving free the binding site for further reaction or it can form cis-COOH again by back reaction with a barrier (TS31) of 17.43 kcal mol⁻¹. The CO₂ to CO conversion along the trans path has a lower energy barrier because the trans-COOH intermediate is more stable than cis-COOH. The CO₂ is converted into trans-COOH with a lower barrier (TS02) of 23.30 kcal mol⁻¹. The reverse process has low barrier (TS20) of 1.11 kcal mol⁻¹ or it can react with another hydrogen from solution to form adsorbed CO with no barrier (TS23). This weakly adsorbed CO is finally evolved from solution as CO gas with the same barrier (TS30), leaving an empty catalysts surface or it can convert into trans-COOH by back reaction with high barrier (TS32) of 14.45 kcal mol⁻¹.

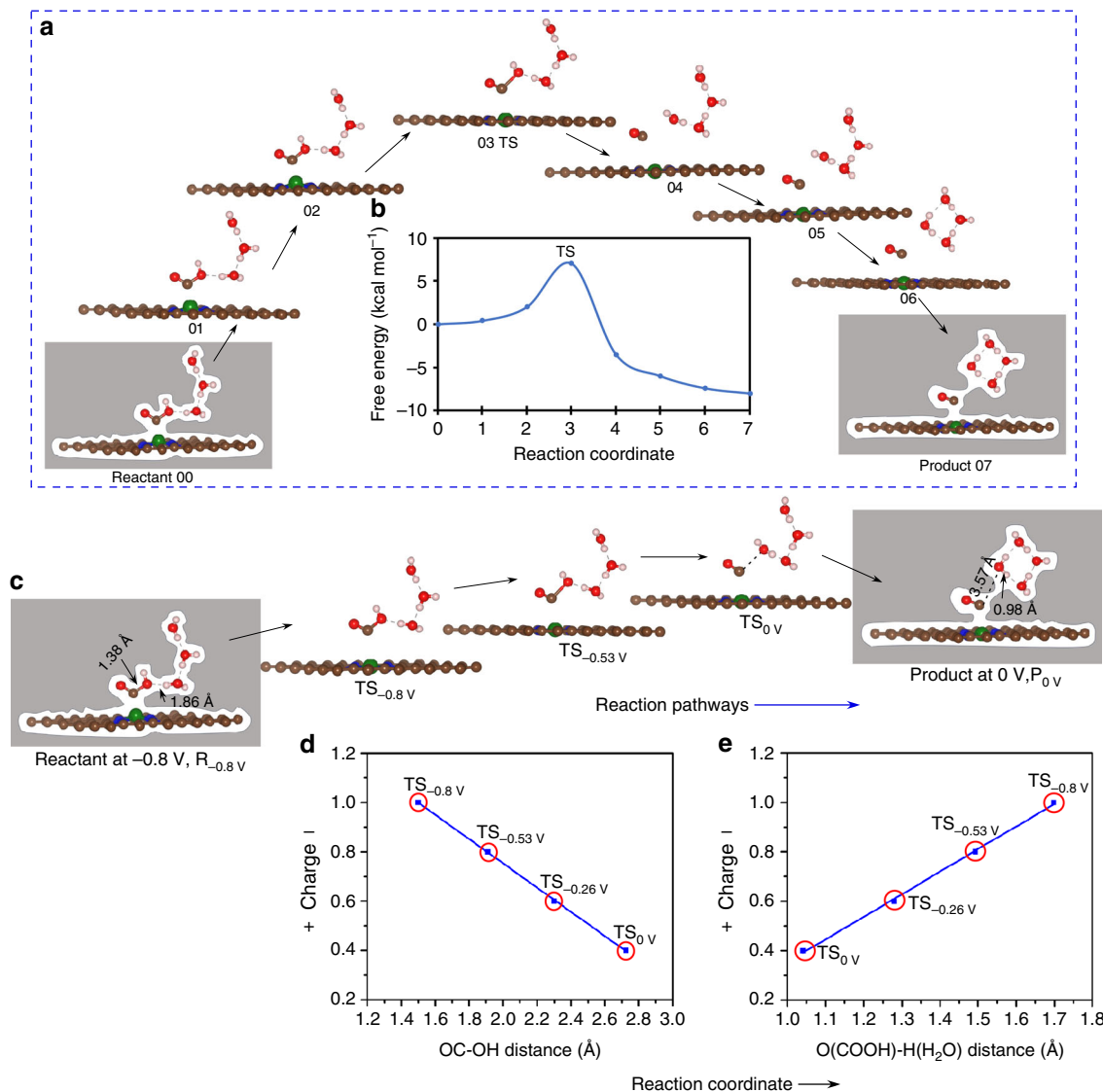


Fig. 4 COOH to CO reaction pathways and transition states at different potential. **a** The minimum energy path (MEP) for cis-COOH to CO conversion at -0.53 V applied potential (0.8 charge) on Ni- N_4 site. We use a total of eight images (00-07) for this conversion process. During the reaction of cis-COOH with water, the OC-OH bond length increases from 1.38 to 1.86 Å with a transition state (TS) at image 03. Eventually it forms CO by breaking OC-OH bond. The arrow indicates the forward direction of the reaction via MEP. **b** The free energy barrier for the cis-COOH to CO at -0.53 V applied potential via MEP. Image 03 (TS) shows the maximum energy barrier of $7.02 \text{ kcal mol}^{-1}$ at -0.53 V applied potential for the conversion of cis-COOH to CO on Ni- N_4 site. **c** The transition state (TS) between reactant cis-COOH and product CO changes with applied potential. Staring from product, at zero applied potential the product (P_{0V}) CO is 3.57 Å (OC-OH) distance away from neighboring water while the O-H bond distance in water is 0.98 Å. The transition state at zero (TS_{0V}) applied potential shows a geometry similar to the product. At -0.53 V applied potential, the OC-OH distance at the transition state ($TS_{-0.53V}$) decreases while the O-H bond increases. With a more negative applied potential of -0.8 V, the OC-OH bond of the transition state ($TS_{-0.8V}$) becomes very early, closer to the reactant at same potential. The reactant at -0.8 V ($R_{-0.8V}$) has OC-OH = 1.38 Å and O-H = 1.86 Å. The arrow indicates the reactant to product direction. **d** The relation of distance between OC-OH to the fractional charge in the TS as a function of applied potential. **e** The change of distance between O-H and the fractional charge in the TS as a function of applied potential. The red circle represents the TS at different applied potentials. (Gray color: entire surface represents implicit solvation along the whole reaction pathways, brown: carbon, blue: nitrogen, green: nickel, red: oxygen, off white: hydrogen atom).

Overall kinetics and comparison with experiments. The Free energies of all reaction intermediates and transition states were calculated as a function of applied potential using our quadratic transformation of the grand canonical potential. Since, the reaction rates depend directly on the applied potential, we obtain the rates from the free energy change to the TS using the Eyring rate equation. Finally, the overall reaction rate and species concentration are calculated using a microkinetic model. The rate equations for each species are as

follows below:

$$\begin{aligned} \frac{dx_0}{dt} &= -(k_{01} + k_{02} + k_{04})x_0 + k_{10}x_1 + k_{20}x_2 + k_{30}x_3 + (k_{40} + k_{l40})x_4 \\ \frac{dx_1}{dt} &= k_{01}x_0 - (k_{10} + k_{13})x_1 + k_{31}x_3 \\ \frac{dx_2}{dt} &= k_{02}x_0 - (k_{20} + k_{23})x_2 + k_{32}x_3 \\ \frac{dx_3}{dt} &= k_{13}x_1 + k_{23}x_2 - (k_{31} + k_{32} + k_{30})x_3 \\ \frac{dx_4}{dt} &= k_{04}x_0 - (k_{40} + k_{l40})x_4 \end{aligned}$$

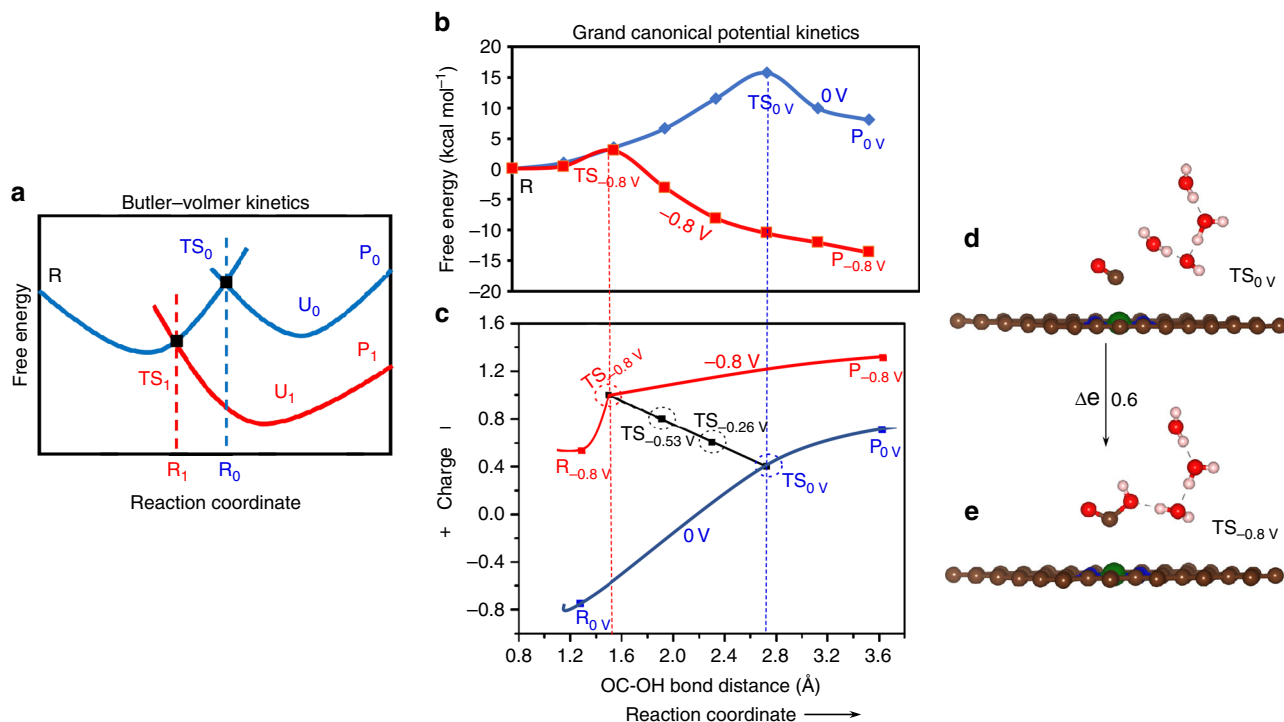


Fig. 5 Schematic and quantitative description of the reaction kinetics. **a** The traditional Butler-Volmer reaction kinetics. Starting from product (blue curves), at zero applied potential, (U_0) the reaction between reactant, R and product, P_0 shows a transition state (TS_0) with R_0 spatial distance along the reaction path. The transition state (TS_1) shifts toward the reactant with lower in free energy gives R_1 spatial distance at applied potential U_1 between reactant R and product P_1 (red curves). The product forms with a single electron transfer from electrode to product, leading an electron transfer jump along the reaction pathway. **b, c** Grand canonical potential kinetics methodology, illustrating the relationship between the TS geometry and charge as the reaction changes continuously with applied potential, leading to a continuous potential dependent reaction path. The blue curve represents the reaction pathways for cis-COOH to CO conversion on Ni- N_4 site at zero (0 V) potential while the red curve is for -0.8 V applied potential. At 0 V, the reaction between reactant, R or R_{0V} and product, P_{0V} produces a transition state (TS_0) with OC-OH = 2.77 Å (blue dotted line) and an energy barrier of 16.89 kcal mol $^{-1}$. At -0.8 V applied potential the energy barrier for the transition state $TS_{-0.8V}$ decreases to 2.98 kcal mol $^{-1}$ with OC-OH = 1.46 Å (red dotted line). The black line connecting the transition states at 0 V (TS_0) and -0.8 V ($TS_{-0.8V}$) shows the linear continuous relation between the applied potential and species charge within the system. The dotted circles indicate the transition states at different applied potentials. **d, e** The geometry of the transition state at zero (TS_0) and -0.8 V ($TS_{-0.8V}$) applied potential, resulting a charge difference of 0.6 e. The arrow represents the TS direction on applied potential. (brown: carbon, blue: nitrogen, green: nickel, red: oxygen, off white: hydrogen atom).

and, the Eyring rate equation for rate constant:

$$k_{ij}(U) = \frac{k_B T}{h} \exp\left(\frac{-\Delta G_{ij}^\ddagger(U)}{k_B T}\right)$$

where, x_i is the concentration of each species, $k_{ij}(U)$ is the potential dependent rate constant, k_B is the Boltzmann's constant, and h is the Planck's constant. Here we apply the constraint $\sum_i x_i = 1$. Solving for the rate at the onset potential for each case, we obtain the concentration of each species as summarized in Table 1.

Solving these equations to obtain the kinetics as a function of applied potential leads to the current density as a function of applied potential shown in Fig. 7b-e for the CO $_2$ reduction reaction. Depending on each reaction rate, the concentrations change as a function of the applied potential. Figure 7b, c shows the CO partial current densities as a function of applied potential for the Ni- N_2C_2 , Ni- N_3C_1 and Ni- N_4 catalysts. The I-V curves show that CO $_2$ RR starts first from Ni- N_2C_2 sites at -0.7 V with U_{onset} (10 mA cm $^{-2}$) = -0.84 V. At $U = -0.84$ V, we calculate the CO faradic efficiency (FE) to be 98% with a turn-over-frequency (TOF) of 3903 h $^{-1}$ per site. We calculate the Tafel slope for Ni- N_2C_2 to be 52 mV dec $^{-1}$ (Fig. 7d), which is

dominated by fast electron transfer followed by a slow protonation step converting CO $_2$ to COOH as the rate limiting step (RDS). We find that for $U < -0.9$ V the current tends to saturate with a very large Tafel slope due to the strong CO bond to the Ni site. For $U < -0.93$ V, Ni- N_3C_1 becomes more active than Ni- N_2C_2 site, which are blocked by strong CO binding (Fig. 7c). For the Ni- N_3C_1 site, we obtain $U_{\text{onset}} = -0.92$ V, FE = 78% and TOF = 2940 h $^{-1}$ with a maximum Tafel slope of 62 mV dec $^{-1}$. The Tafel slope drastically increases for $U < -1.06$ V due to strong CO bonding to Ni site. Then as $U < -1.05$ V, Ni- N_4 dominates CO production. For Ni- N_4 , we find $U_{\text{onset}} = -1.03$ V with a high FE = 99%, and TOF = 3944 h $^{-1}$ with a Tafel slope of 55 mV dec $^{-1}$. Here the binding of CO to the Ni is weaker, so that very high currents are predicted (this may be limited by transport and other issues). Overall, the Ni- N_2C_2 site dominates CO production for $U \sim -0.85$ V, with Ni- N_3C_1 dominating by -0.95 V, and Ni- N_4 dominating by -1.12 V. For comparison, Fig. 7b shows the experimental data for CO $_2$ RR from three papers, normalized (Supplementary Note 3) to have the same active sites concentrations^{21,25,27}. The recent experimental papers lead to an onset potential at 10 mA cm $^{-2}$ of -0.7 , -0.84 , and -0.93 V in reasonable agreement with our predictions for the Ni- N_2C_2 site ($U_{\text{onset}} = -0.84$ V) and Ni- N_3C_1 site ($U_{\text{onset}} = -0.92$ V)^{20,25,27,28,49}.

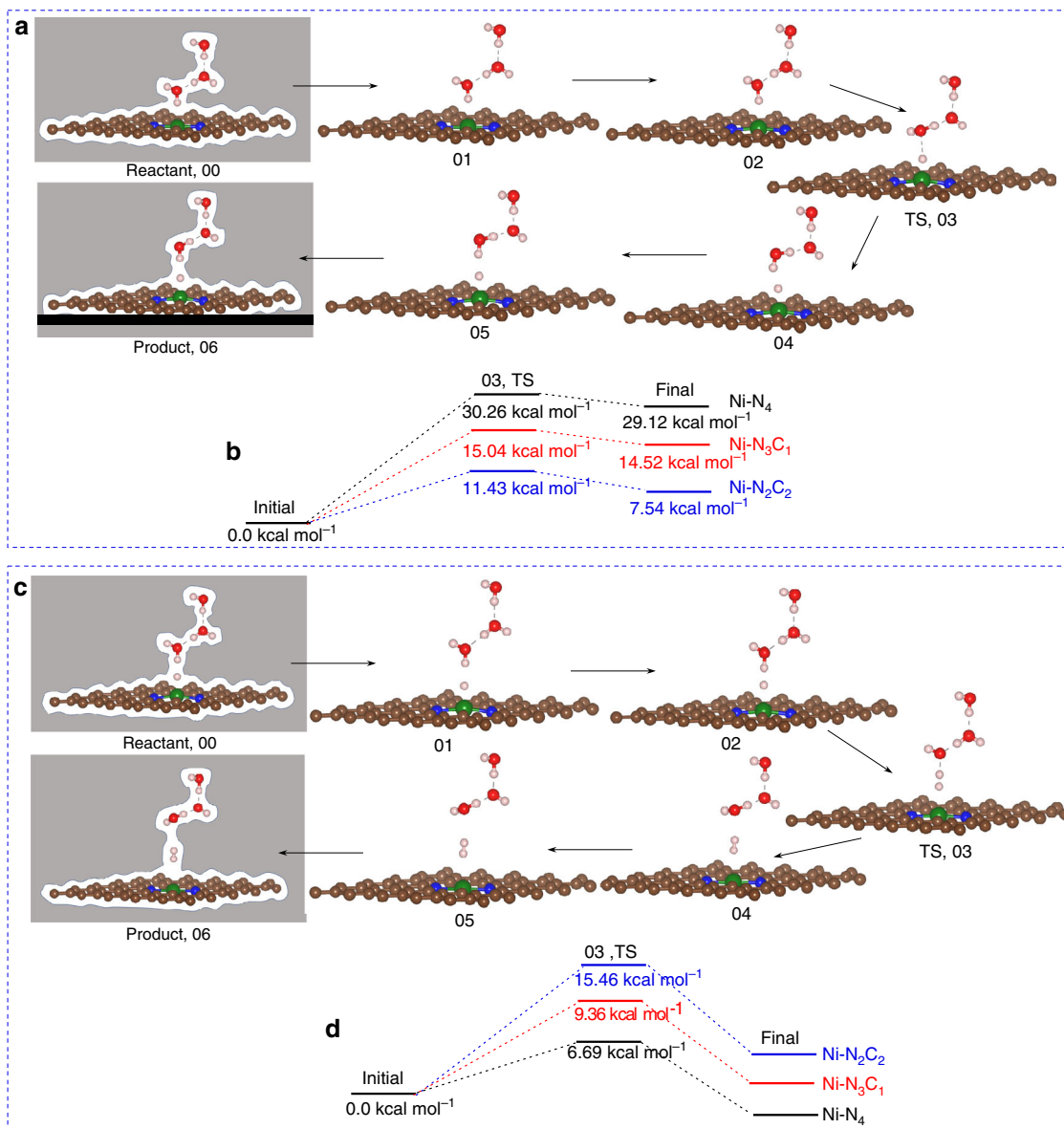


Fig. 6 Reaction pathways for hydrogen evolution reaction (HER) on nickel single site. **a** The minimum energy reaction path for proton adsorption (Volmer step) from solution to the nickel single site at -0.8 V applied potential. We use total seven images (00–06) for this adsorption step. The hydrogen near the single nickel at point 00 gradually moves toward the nickel site leading to a transition state (TS) at 03 before converting into the adsorbed final state at 06. **b** The adsorption free energies and TS barrier for the Volmer step of HER on different nickel sites at -0.8 V vs RHE applied potential. Among all sites, Ni-C₂N₂ shows a lower activation barrier for proton transfer at the active site. **c** The Heyrovsky reaction path for hydrogen gas evolution from the nickel surface at -0.8 V applied potential. We use seven images (00–06) to describe the H₂ desorption step. The adsorbed hydrogen at point 00 reacts with a proton from solution to form H₂ gas at 06, leading to a transition state at point 03. **d** Desorption reaction barrier for the Heyrovsky step of HER on different nickel sites at -0.8 V vs RHE applied potential. The H₂ evolution is difficult from Ni-C₂N₂ site because its strong adsorption energy for the Volmer step. The arrow indicates the forward reaction pathways for adsorption and desorption steps, respectively. (Gray color: entire surface represents implicit solvation along the whole reaction pathways, brown: carbon, blue: nitrogen, green: nickel, red: oxygen, off white: hydrogen atom).

Thus, we conclude that experimental Ni-SACs may have all three sites in different proportions contributing to the overall CO₂ reduction performance.

The I-V curves for HER are shown in Fig. 7e. Most notable is that HER for Ni-N₃C₁ site starts at $U = -0.72$ V, reaches 5 mA cm^{-2} at -0.96 V, and 10 mA cm^{-2} at -1.09 V. In contrast HER for Ni-N₂C₂ and Ni-N₄ do not start until $U < -0.98$ V. This suggests that to reduce HER the synthesis should attempt to minimize Ni-N₃C₁ sites and use applied potentials less negative than $U = -1.0$ V where CO performance is reasonably high. The Tafel slopes obtained for HER on Ni-N₂C₂ sites is 100 mV dec^{-1}

and for Ni-N₃C₁ it is 153 mV dec^{-1} (Supplementary Fig. 13). This can be compared to the experimental value of 140 mV dec^{-1} ²⁵. For Ni-N₄ site, HER is very slow, leading to $U_{\text{onset}} = -1.31$ V for 10 mA cm^{-2} , with a Tafel slope 84 mV dec^{-1} . Thus Ni-N₄ is the best overall performer with a current of 40 mA cm^{-2} at $U = -1.05$ V with CO FE $\sim 100\%$.

Comparison of QM based descriptors with experiments. In order to find the synthesis conditions that maximize production of the desired sites, say Ni-N₄ it would be useful to have descriptors indicating which sites dominate prior to

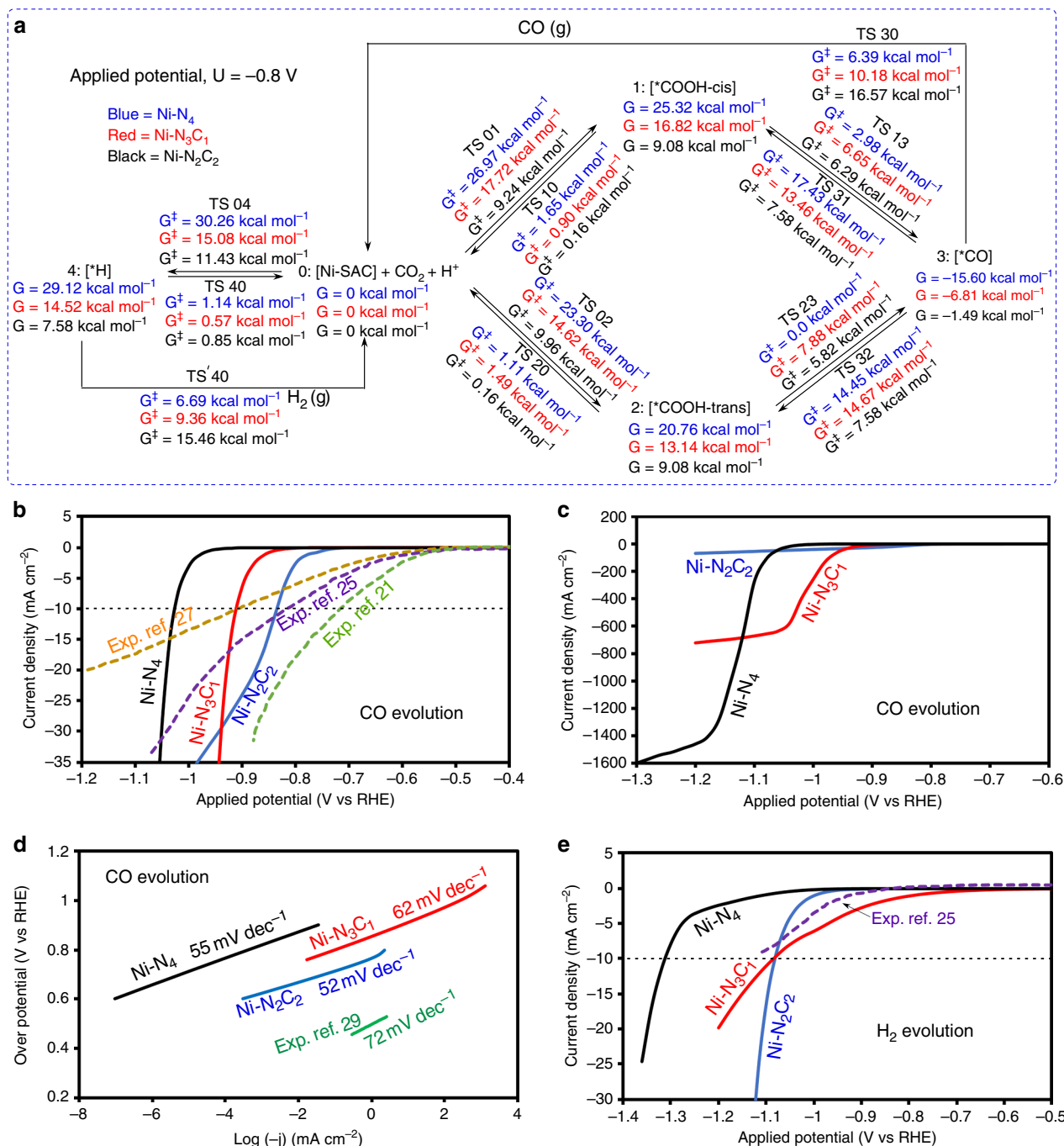


Fig. 7 QM derived free energies and predicted reaction kinetics. **a** Schematic representation of free energies at 298 K and pH 7 for -0.8 V applied potential. This summarizes all reaction intermediates (0–4) and transition state (TS) free energies involved in the reduction of CO₂ on nickel single site at -0.8 V constant applied potential. (Blue: Ni-N₄, Red: Ni-N₃C₁ and Black: Ni-N₂C₂ surface). **b** Calculated partial current densities for CO evolution during CO₂ reduction on Ni-N₂C₂ (blue curve), Ni-N₃C₁ (red curve) and Ni-N₄ (black curve) along with experimental data from refs. 21,25,27 (dotted curve) for comparison (equivalent number of nickel atoms). **c** Large partial current densities for CO evolution during CO₂ reduction on Ni-N₂C₂ (blue curve), Ni-N₃C₁ (red curve) and Ni-N₄ (black curve). **d** Tafel slopes calculated from the I–V curves for CO evolution on Ni-N₂C₂ (blue line), Ni-N₃C₁ (red line) and Ni-N₄ (black line) during CO₂ reduction, showing good agreement with the Tafel slope from experiment (green line). **e** Calculated partial H₂ current densities as a function of applied potential during CO₂ reduction on Ni-N₂C₂ (blue curve), Ni-N₃C₁ (red curve) and Ni-N₄ (black curve) along with experimental data from ref. 25 (dotted curve) for comparison (equivalent number of nickel atoms), at pH 7 and 298 K.

experimentally inserting into a cell. The CO stretching vibration is prominent in the FT-IR, occurring experimentally at 1900–2060 cm⁻¹ on Ni single sites⁵⁰. We calculated the vibration wavenumbers for adsorbed CO on different Ni-sites at applied potentials corresponding to high adsorbed CO concentrations (Supplementary Fig. 14). We found that $U = -1.0$ V leads to the

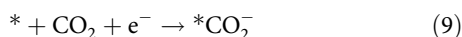
highest amount of CO adsorbed on Ni-N₂C₂ moiety, leading to 1985 cm⁻¹ with vertical polarization. For Ni-N₃C₁, the highest CO concentration is for $U = -1.1$ V, leading to 1959 cm⁻¹ while for Ni-N₄, the highest CO concentration is for $U = -1.25$ V leading to 1942 cm⁻¹. Both latter cases lead to CO polarization off from vertical. Our calculated values are in the range of

experiment and the dependence on site is sufficiently large to identify which Ni sites are present. Additionally, we used QM calculation to predict XPS BE shifts for N 1s to identify how many nitrogens are bonded to Ni in Ni-SACs. The experimentally deconvoluted N 1s peaks indicate several nitrogen moieties, but only pyridinic nitrogen bonded to Ni shows a shift from normal pyridinic N BE value. The experimental BE difference between pyridinic N and M-N_x varies from 0.9 to 1.3 eV.

So, we took pyridinic N 1s as reference BE for comparing the BE shifts. The BE shift, ΔBE for N 1s is 0.96 eV (lowest) for Ni-N₂C₂ site and 1.18 eV (highest) for Ni-N₄ site, which are in the range of experiment (Table 2). We found that the C 1s BE decreases to 0.62 eV and 1.21 eV for Ni-N₃C₁ and Ni-N₂C₂. Finally, we also observed that the Ni 2p BE shift is 0.28 eV for Ni-N₂C₂ (lowest) and 0.90 eV for Ni-N₄ site (highest). These differences might be too small to be resolved experimentally.

Discussion

The CO₂ reduction to CO involves four steps. Firstly, linear CO₂ binds to the catalysts surface (*) by forming bent *CO₂⁻ via electron transfer



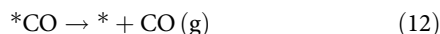
then hydrogen transfer from water converts bent CO₂ into adsorbed *COOH intermediate plus solvated OH⁻



then a second hydrogen transfer from water converts adsorbed *COOH intermediate into bound CO plus H₂O plus solvated OH⁻



Finally, the bound *CO desorbs from the catalyst surface as CO gas, and making the surface empty (*) for further reaction



The Tafel slope provides an indication of the rate determining step for this reaction. According to Butler-Volmer equation, Tafel

slopes should be around 120, 60, 40 mV dec⁻¹, and ∞ if the rate determining steps are (9), (10), (11), and (12), respectively. We calculated Tafel slopes of 52, 62, and 55 mV dec⁻¹ for Ni-N₂C₂, Ni-N₃C₁ and Ni-N₄, respectively, obtained near to their onset potential, U_{onset}.

Our calculations show that CO₂ activation is easier due to presence of Ni⁺ instead of Ni²⁺, where the highest occupied molecular orbital (HOMO) of Ni⁺ in Ni-SACs (Ni 3d_{x₂-y₂} rather than 3d_{z²} for Ni²⁺) has tendency to overlap with the C 2p* orbital in CO₂. Thus, protonation of *CO₂⁻ to become *COOH leads to the highest energy barrier (Figs. 3 and 7), which is the RDS for all active sites we studied. This should lead to Tafel slope ~60 mV dec⁻¹. Recently, Gu et al.⁵² observed that the initial electron for reduction of CO₂ is decoupled from a proton transfer on Fe³⁺-N-C and found that CO₂ adsorption is fast, and the rate limiting step is protonation of the adsorbed CO₂⁻ to form an adsorbed COOH intermediate, with an experimental Tafel slope of 64 mV dec⁻¹. Moreover, experiments by Liu et al.²⁹ for CO₂RR on a Ni-single atom catalyst confirmed the presence of Ni⁺ by operando spectroscopic characterization. They observed that the proton transfer to the adsorbed *CO₂ is the rate determining step with a Tafel slope of 72 mV dec⁻¹. Thus the experiments lead to Tafel slope very close to the 62 mV dec⁻¹ we calculate for Ni-N₃C₁.

It has been shown experimentally⁴⁹ that Ni-single atom catalysts can deliver a large current density of 220 mA cm⁻² at -1.0 V RHE with 88.5% FE. We predict that our most active site at -1.0 V, Ni-N₃C₁, leads to a CO current of 259 mA cm⁻², slightly higher than experiment (192 mA cm⁻²). This may be due to mass transport issues that we ignore. According to Singh et al.^{53,54} at higher negative potential (-1.0 V vs RHE), the transport of CO₂ to the catalyst and the transport of OH⁻ anions away from the catalyst become rate limiting due to cathodic polarization. Moreover, as a consequence of the latter effect, the pH near the catalyst surface rises well above 7, and the concentration of CO₂ decreases dramatically because of the reaction of CO₂ with OH⁻ anions to form HCO₃⁻ and CO₃⁻ anions. The net effect is to alter the current-voltage profile significantly.

The double layer capacitance is an important parameter that can affect the current-voltage relations for CO₂ reduction. The double layer capacitance arises from charge transfer in contact between the conductive electrode and the electrolytic solution. Experimentally, the double layer capacitance, C_{diff}, is between 20 and 25 μF cm⁻² for most metal surfaces. Ringe et al.⁵⁵ assumed a value of 25 μF cm⁻² in their model to address double layer effects for CO₂ reduction reaction on Ag (111) single crystal electrode. As described earlier, the GCP-K leads directly to a differential capacitance, C_{diff}, that can be compared to experiment. The values for various intermediates are shown in Table 3. We found that the capacity differences, C_{diff} are 12–29 μF cm⁻² for Ni-N₂C₂, 12–20 μF cm⁻² for Ni-N₃C₁, and 13–22 μF cm⁻² for Ni-N₄ system, close to the observed values (20–25 μF cm⁻²) reported experimentally^{56,57}. This further validates our methodology for catalyst-electrolyte interface. We also calculated the PZC and F₀ value for each of reaction intermediates for the various active sites (Supplementary Tables 3–5).

Table 1 Species concentration corresponding to the onset potential of each site at 298 K and pH = 7.

Species	Conc. (Ni-N ₂ C ₂)	Conc. (Ni-N ₃ C ₁)	Conc. (Ni-N ₄)
[Ni-SAC] (x ₀)	0.88736	0.92943	0.99165
[*cis-COOH] (x ₁)	8.769 × 10 ⁻⁰⁵	4.051 × 10 ⁻⁰⁴	6.471 × 10 ⁻⁰⁸
[*trans-COOH] (x ₂)	3.221 × 10 ⁻⁰⁶	1.199 × 10 ⁻⁰⁴	1.111 × 10 ⁻⁰⁶
[*CO] (x ₃)	0.11259	0.07003	0.00835
[*H] (x ₄)	2.5616 × 10 ⁻⁰⁵	5.087 × 10 ⁻⁰⁵	1.649 × 10 ⁻⁰⁸
Onset potential, U _{onset} for 10 mA cm ⁻²	-0.84 V	-0.92 V	-1.03 V

The sum of all species concentrations is 1.

Table 2 QM derived binding energy shift for N 1s for different bonding sites with nickel.

Type of Ni-sites	Reference value	Ni-N ₂ C ₂	Ni-N ₃ C ₁	Ni-N ₄	Graphitic N
Calculated ΔBE, eV for N 1s	0 (pyridinic N)	+0.96	+1.05	+1.18	+2.76
Experimental ^{16,20,26,51}	398.0–398.5 eV	+0.9–1.3	+2.5–3.5		
Calculated BE shift for C 1s	0 (graphene)	-1.21	-0.62	-	-
Calculated BE shifts for Ni 2p	0 (Ni atom)	+0.28	+0.50	+0.90	-

Table 3 Calculated differential capacitance for different intermediates during CO₂ reduction reaction.

Species	Differential Capacitance, C _{diff}		
	Ni-N ₂ C ₂	Ni-N ₃ C ₁	Ni-N ₄
Empty sites	15.87	20.06	17.02
CO ₂	29.00	19.85	14.88
Cis-COOH	22.66	15.24	21.93
Trans-COOH	23.79	14.64	20.30
CO	12.34	16.98	14.38
TS01	22.88	13.34	21.98
TS02	23.21	13.25	23.85
TS13	14.01	13.73	13.38
TS23	14.28	12.36	15.56
[Ni-SAC]H	15.87	13.20	19.43
[Ni-SAC]H ₂	14.91	12.70	14.30

In conclusion, we examined the reaction mechanism and kinetics for the reduction of CO₂ over graphene-supported Ni-single atom catalysts (Ni-SACs) using the new grand canonical potential kinetics (GCP-K) formulation. This allows the geometry of the transition states and the charge transfer from electrode to adsorbed species to change continuously along the reaction coordinates as the potential is changed. GCP-K describes the electron transfer accompanying proton or hydrogen transfer as a continuous process, rather than as a discrete electron jump as in the PCET formulation of traditional Butler–Volmer kinetics.

We applied the GCP-K method to determine the reaction mechanism and kinetics for CO₂RR on all three Ni sites: Ni-N₂C₂, Ni-N₃C₁, and Ni-N₄ likely to be present in Ni-SACs. We find each site leads to unique kinetics with Ni-N₂C₂ dominant for $-0.93 < U < -0.75$ V, producing 10 mA cm⁻² current density at $U_{\text{onset}} = -0.84$ V, with a Tafel slope of 52 mV dec⁻¹, a faradic efficiency (FE) of 98%, and TOF = 3903 h⁻¹ per Ni site. On the other hand, Ni-N₃C₁ dominant for $-1.05 < U < -0.93$ V producing 10 mA cm⁻² current density at $U_{\text{onset}} = -0.92$ V, with a Tafel slope of 62 mV dec⁻¹, a FE = 78% and TOF = 2940 h⁻¹ per Ni site while Ni-N₄ dominant for $U < -1.05$ V producing 10 mA cm⁻² current density at $U_{\text{onset}} = -1.03$ V with a Tafel slope of 55 mV dec⁻¹, a FE = 99% faradic efficiency, and TOF = 3944 h⁻¹ per Ni site. These predicted overall kinetics show reasonable agreement with experimental studies. Thus ref. ^{25,27} leads to CO dependence on U similar to what we find for Ni-N₂C₂. We find that HER activity on Ni-SAC depends very much on the site, with HER on Ni-N₃C₁ starting at $U = -0.8$ V. The Ni-N₄ leads to the best overall performance for CO₂ reduction: At $U = -1.05$ V we find 40 mA cm⁻² with CO FE ~ 100%.

In order to help guide identification of the sites in experimental synthesized Ni-SACs, we predicted the XPS N and C 1s and Ni 2p BE shift and the CO vibrational frequencies for various sites. We find that the pyridinic N 1s XPS binding shifts is highest (+1.18 eV) for Ni-N₄ and lowest (+0.96 eV) for Ni-N₂C₂. While the C 1s shift is -0.62 for Ni-N₃C₁ and -1.21 eV for Ni-N₂C₂. Finally, The Ni 2p BE shift is +0.90 eV (maximum) for Ni-N₄ and +0.28 eV (minimum) for Ni-N₂C₂ site. The CO stretch for CO bound to Ni is 1985 cm⁻¹ at -1.0 V on Ni-N₂C₂ site and 1942 cm⁻¹ at -1.25 V on Ni-N₄ site. These predicted results for Ni-N₂C₂ site agree best with experiment, but we expect that most synthesized catalysts have mixtures of all three Ni sites so that the total CO current for arises from each of them.

Methods

Computational details. The geometry optimization was performed as a function of constant charge using the PBE-D3 functional^{58–60} with VASPsol^{61,62} implemented

in VASP^{63–65} and including spin polarization (Supplementary Note 2). Then we used the Legendre transformation to transform the VASP results to constant potential followed by using the CANDLE solvation model³⁵ (as implemented in jDFTx v.1.2.1)⁶⁶ for the final constant potential results. Here we included a few waters to describe explicitly the polarization involved in proton transfer. The positions of these waters were optimized with VASPsol. For the reaction barriers we did free energy calculation for each point along the NEB reaction path using VASPsol, so that the geometry of the transition state could change adiabatically as a function of applied potential. The VTST package⁶⁷ with climbing image nudged elastic band (CI-NEB)⁶⁸ was used to obtain the reaction pathway and transition states including solvation.

We used a plane wave basis set with 500 eV cutoff energy. The geometry optimization criteria were set to 10⁻⁶ eV for energy and 0.01 eV Å⁻¹ for forces on each atom while for CI-NEB we used 0.02 eV Å⁻¹. A Gaussian smearing of 0.05 eV was applied throughout the whole calculation. The K-points were selected to be 5 × 5 × 1 for structure relaxation and energy calculations. The graphene unit cell dimensions were optimized to be 2.46 Å × 2.46 Å with 20 Å distance between layers perpendicular to the surface. Finally, 4 × 4 super cells of graphene were used with 26 carbon atoms and 1 metal atom placed on the carbon divacancy.

The single point jDFTx calculations were used to obtain the combined DFT and solvation free energy using the geometry optimized with VASPsol. The jDFTx calculation was chosen because of the accuracy in describing continuum solvation and for including constant potentials for electrochemical reaction. But we found that a single point calculation is sufficient for the stable species since the structures observed are similar in both VASPsol and jDFTx (Supplementary Table 6). The CANDLE solvation model was used in jDFTx to describe solvation implicitly. Using this scheme, $\mu_{e,\text{SHE}} = 4.66$ eV, which was used for all structures. A plane wave basis set with energy cutoff of 20 Hartree was used with a k-point mesh of 5 × 5 × 1. The free energy convergence criteria were set to 10⁻⁸ Hartree.

XPS BE shift calculations were performed using the core level energies implemented in VASP⁶³. There are two methods for such calculations; we used simpler option (ICORELEVEL = 1) to calculate the core levels in the initial state approximation. This is based on the observation in recent publications that this method leads relative BE shifts in good agreement with experimental XPS^{69,70}. This method involves recalculating the KS eigenvalues of the core states after a self-consistent calculation of the valence charge density. The phonon density of states were calculated using VASP by setting IBRION = 5 in the INCAR file. The Hessian matrix and the vibrational frequencies of a system were calculated using atom displacements in all three cartesian directions with a step size of 0.015 Å (POTIM). We allowed only the adsorbed molecule to vibrate and the vibrational frequencies were taken from the normal mode analysis. To calculate entropy, we used the phonon density of states, as found in OUTCAR as “f” on the real axis. Then we extracted total vibrational ZPE, enthalpy, and entropy.

Data availability

The data that support the findings of this study are available from the corresponding author upon request.

Received: 30 September 2019; Accepted: 7 April 2020;

Published online: 07 May 2020

References

- Turner, J. A. A realizable renewable energy future. *Science* **285**, 687 (1999).
- Chu, S. & Majumdar, A. Opportunities and challenges for a sustainable energy future. *Nature* **488**, 294–303 (2012).
- Wang, Y. et al. Paleo-CO₂ variation trends and the Cretaceous greenhouse climate. *Earth Sci. Rev.* **129**, 136–147 (2014).
- Sun, Z., Ma, T., Tao, H., Fan, Q. & Han, B. Fundamentals and challenges of electrochemical CO₂ reduction using two-dimensional materials. *Chem* **3**, 560–587 (2017).
- Gao, S. et al. Partially oxidized atomic cobalt layers for carbon dioxide electroreduction to liquid fuel. *Nature* **529**, 68–71 (2016).
- Voiry, D., Shin, H. S., Loh, K. P. & Chhowalla, M. Low-dimensional catalysts for hydrogen evolution and CO₂ reduction. *Nat. Rev. Chem.* **2**, 0105 (2018).
- Ooka, H., Figueiredo, M. C. & Koper, M. T. M. Competition between hydrogen evolution and carbon dioxide reduction on copper electrodes in mildly acidic media. *Langmuir* **33**, 9307–9313 (2017).
- Whipple, D. T. & Kenis, P. J. A. Prospects of CO₂ utilization via direct heterogeneous electrochemical reduction. *J. Phys. Chem. Lett.* **1**, 3451–3458 (2010).
- Zhu, W. et al. Monodisperse Au nanoparticles for selective electrocatalytic reduction of CO₂ to CO. *J. Am. Chem. Soc.* **135**, 16833–16836 (2013).
- Li, C. W. & Kanan, M. W. CO₂ reduction at low overpotential on Cu electrodes resulting from the reduction of thick Cu₂O films. *J. Am. Chem. Soc.* **134**, 7231–7234 (2012).

11. Cheng, T., Xiao, H. & Goddard, W. A. Reaction mechanisms for the electrochemical reduction of CO₂ to CO and formate on the Cu(100) surface at 298 K from quantum mechanics free energy calculations with explicit water. *J. Am. Chem. Soc.* **138**, 13802–13805 (2016).
12. Sarfraz, S., Garcia-Esparza, A. T., Jedidi, A., Cavallo, L. & Takanabe, K. Cu–Sn bimetallic catalyst for selective aqueous electroreduction of CO₂ to CO. *ACS Catal.* **6**, 2842–2851 (2016).
13. Kim, D., Resasco, J., Yu, Y., Asiri, A. M. & Yang, P. Synergistic geometric and electronic effects for electrochemical reduction of carbon dioxide using gold–copper bimetallic nanoparticles. *Nat. Commun.* **5**, 4948 (2014).
14. Cheng, T., Huang, Y., Xiao, H. & Goddard, W. A. Predicted structures of the active sites responsible for the improved reduction of carbon dioxide by gold nanoparticles. *J. Phys. Chem. Lett.* **8**, 3317–3320 (2017).
15. Fei, H. et al. Atomic cobalt on nitrogen-doped graphene for hydrogen generation. *Nat. Commun.* **6**, 8668 (2015).
16. Hossain, M. D. et al. Rational design of graphene-supported single atom catalysts for hydrogen evolution reaction. *Adv. Energy Mater.* **9**, 1803689 (2019).
17. Yang, L. et al. Unveiling the high-activity origin of single-atom iron catalysts for oxygen reduction reaction. *Proc. Natl Acad. Sci. USA* **115**, 6626–6631 (2018).
18. Chen, Y. et al. Enhanced oxygen reduction with single-atomic-site iron catalysts for a zinc-air battery and hydrogen-air fuel cell. *Nat. Commun.* **9**, 5422 (2018).
19. Back, S., Lim, J., Kim, N.-Y., Kim, Y.-H. & Jung, Y. Single-atom catalysts for CO₂ electroreduction with significant activity and selectivity improvements. *Chem. Sci.* **8**, 1090–1096 (2017).
20. Ju, W. et al. Understanding activity and selectivity of metal-nitrogen-doped carbon catalysts for electrochemical reduction of CO₂. *Nat. Commun.* **8**, 944 (2017).
21. Yang, H. B. et al. Atomically dispersed Ni(i) as the active site for electrochemical CO₂ reduction. *Nat. Energy* **3**, 140–147 (2018).
22. Liu, M., Zhang, R. & Chen, W. Graphene-supported nanoelectrocatalysts for fuel cells: synthesis, properties, and applications. *Chem. Rev.* **114**, 5117–5160 (2014).
23. Li, Y. et al. MoS₂ nanoparticles grown on graphene: an advanced catalyst for the hydrogen evolution reaction. *J. Am. Chem. Soc.* **133**, 7296–7299 (2011).
24. Chen, Y. et al. Single-atom catalysts: synthetic strategies and electrochemical applications. *Joule* **2**, 1242–1264 (2018).
25. Jiang, K. et al. Isolated Ni single atoms in graphene nanosheets for high-performance CO₂ reduction. *Energy Environ. Sci.* **11**, 893–903 (2018).
26. Yan, C. et al. Coordinatively unsaturated nickel–nitrogen sites towards selective and high-rate CO₂ electroreduction. *Energy Environ. Sci.* **11**, 1204–1210 (2018).
27. Zhao, C. et al. Ionic exchange of metal–organic frameworks to access single nickel sites for efficient electroreduction of CO₂. *J. Am. Chem. Soc.* **139**, 8078–8081 (2017).
28. Su, P., Iwase, K., Nakanishi, S., Hashimoto, K. & Kamiya, K. Nickel-nitrogen-modified graphene: an efficient electrocatalyst for the reduction of carbon dioxide to carbon monoxide. *Small* **12**, 6083–6089 (2016).
29. Liu, S. et al. Elucidating the electrocatalytic CO₂ reduction reaction over a model single-atom nickel catalyst. *Angew. Chem. Int. Ed. Engl.* **59**, 798–803 (2020).
30. Sundararaman, R., Goddard III, W. A. & Arias, T. A. Grand canonical electronic density-functional theory: Algorithms and applications to electrochemistry. *J. Chem. Phys.* **146**, 114104 (2017).
31. Huang, Y., Nielsen, R. J. & Goddard, W. A. Reaction mechanism for the hydrogen evolution reaction on the basal plane sulfur vacancy site of MoS₂ using grand canonical potential kinetics. *J. Am. Chem. Soc.* **140**, 16773–16782 (2018).
32. Sha, Y., Yu, T. H., Merinov, B. V. & Goddard, W. A. Prediction of the dependence of the fuel cell oxygen reduction reactions on operating voltage from DFT calculations. *J. Phys. Chem. C* **116**, 6166–6173 (2012).
33. Jinnouchi, R. & Anderson, A. B. Electronic structure calculations of liquid-solid interfaces: combination of density functional theory and modified Poisson-Boltzmann theory. *Phys. Rev. B* **77**, 245417 (2008).
34. Gunceler, D., Letchworth-Weaver, K., Sundararaman, R., Schwarz, K. A. & Arias, T. A. The importance of nonlinear fluid response in joint density-functional theory studies of battery systems. *Model. Simul. Mater. Sci. Eng.* **21**, 074005 (2013).
35. Sundararaman, R. & Goddard, W. A. The charge-asymmetric nonlocally determined local-electric (CANDLE) solvation model. *J. Chem. Phys.* **142**, 064107 (2015).
36. Goodpaster, J. D., Bell, A. T. & Head-Gordon, M. Identification of possible pathways for C–C bond formation during electrochemical reduction of CO₂: new theoretical insights from an improved electrochemical model. *J. Phys. Chem. Lett.* **7**, 1471–1477 (2016).
37. Xiao, H., Cheng, T., Goddard, W. A. & Sundararaman, R. Mechanistic explanation of the pH dependence and onset potentials for hydrocarbon products from electrochemical reduction of CO on Cu (111). *J. Am. Chem. Soc.* **138**, 483–486 (2016).
38. Chan, K. & Nørskov, J. K. Potential dependence of electrochemical barriers from ab initio calculations. *J. Phys. Chem. Lett.* **7**, 1686–1690 (2016).
39. Taylor, C. D., Wasileski, S. A., Filhol, J.-S. & Neurock, M. First principles reaction modeling of the electrochemical interface: consideration and calculation of a tunable surface potential from atomic and electronic structure. *Phys. Rev. B* **73**, 165402 (2006).
40. Taylor, C. D. & Neurock, M. Theoretical insights into the structure and reactivity of the aqueous/metal interface. *Curr. Opin. Solid State Mater. Sci.* **9**, 49–65 (2005).
41. Mamatkulov, M. & Filhol, J. S. An ab initio study of electrochemical vs. electrochemical properties: the case of CO adsorbed on a Pt(111) surface. *Phys. Chem. Chem. Phys.* **13**, 7675–7684 (2011).
42. Fei, H. et al. General synthesis and definitive structural identification of MN₄C₄ single-atom catalysts with tunable electrocatalytic activities. *Nat. Catal.* **1**, 63–72 (2018).
43. Lin, W., Stocker, K. M. & Schatz, G. C. Mechanisms of hydrogen-assisted CO₂ reduction on nickel. *J. Am. Chem. Soc.* **139**, 4663–4666 (2017).
44. Zhao, Z., Chen, Z. & Lu, G. Computational discovery of nickel-based catalysts for CO₂ reduction to formic acid. *J. Phys. Chem. C* **121**, 20865–20870 (2017).
45. Akhade, S. A. et al. Poisoning effect of adsorbed CO during CO₂ electroreduction on late transition metals. *Phys. Chem. Chem. Phys.* **16**, 20429–20435 (2014).
46. v. Neumann, J. Zur Theorie der Gesellschaftsspiele. *Mathematische Annalen*. **100**, 295–320 (1928).
47. Sato, N. in *Electrochemistry at metal and semiconductor electrodes* (ed. Sato, N.) 213–233 (Elsevier Science, 1998).
48. Bard, A. J. & Faulkner, L. R. *Electrochemical Methods: Fundamentals and Applications* (Wiley, 2000).
49. Möller, T. et al. Efficient CO₂ to CO electrolysis on solid Ni–N–C catalysts at industrial current densities. *Energy Environ. Sci.* **12**, 640–647 (2019).
50. Vogt, C. et al. Unravelling structure sensitivity in CO₂ hydrogenation over nickel. *Nat. Catal.* **1**, 127–134 (2018).
51. Artyushkova, K. et al. Density functional theory calculations of XPS binding energy shift for nitrogen-containing graphene-like structures. *Chem. Commun.* **49**, 2539–2541 (2013).
52. Gu, J., Hsu, C.-S., Bai, L., Chen, H. M. & Hu, X. Atomically dispersed Fe³⁺ sites catalyze efficient CO₂ electroreduction to CO. *Science* **364**, 1091 (2019).
53. Singh, M. R., Clark, E. L. & Bell, A. T. Effects of electrolyte, catalyst, and membrane composition and operating conditions on the performance of solar-driven electrochemical reduction of carbon dioxide. *Phys. Chem. Chem. Phys.* **17**, 18924–18936 (2015).
54. Singh, M. R., Goodpaster, J. D., Weber, A. Z., Head-Gordon, M. & Bell, A. T. Mechanistic insights into electrochemical reduction of CO₂ over Ag using density functional theory and transport models. *Proc. Natl Acad. Sci. USA* **114**, E8812 (2017).
55. Ringe, S. et al. Understanding cation effects in electrochemical CO₂ reduction. *Energy Environ. Sci.* **12**, 3001–3014 (2019).
56. Hamelin, A., Vitanov, T., Sevastyanov, E. & Popov, A. The electrochemical double layer on sp metal single crystals: the current status of data. *J. Electroanal. Chem. Interfacial Electrochem.* **145**, 225–264 (1983).
57. Valette, G. Double layer on silver single crystal electrodes in contact with electrolytes having anions which are slightly specifically adsorbed: Part II. The (100) face. *J. Electroanal. Chem. Interfacial Electrochem.* **138**, 37–54 (1982).
58. Grimme, S., Antony, J., Ehrlich, S. & Krieg, H. A consistent and accurate ab initio parametrization of density functional dispersion correction (DFT-D) for the 94 elements H–Pu. *J. Chem. Phys.* **132**, 154104 (2010).
59. Kresse, G. & Hafner, J. Ab initio molecular dynamics for liquid metals. *Phys. Rev. B* **47**, 558–561 (1993).
60. Kresse, G. & Hafner, J. Ab initio molecular-dynamics simulation of the liquid-metal—amorphous-semiconductor transition in germanium. *Phys. Rev. B* **49**, 14251–14269 (1994).
61. Mathew, K., Sundararaman, R., Letchworth-Weaver, K., Arias, T. A. & Hennig, R. G. Implicit solvation model for density-functional study of nanocrystal surfaces and reaction pathways. *J. Chem. Phys.* **140**, 084106 (2014).
62. Mathew, K., Chaitanya Kolluru, V. S., Mula, S., Steinmann, S. N. & Hennig, R. G. Implicit self-consistent electrolyte model in plane-wave density-functional theory. *J. Chem. Phys.* **151**, 234101 (2019).
63. Kresse, G. & Furthmüller, J. Efficiency of ab-initio total energy calculations for metals and semiconductors using a plane-wave basis set. *Comput. Mater. Sci.* **6**, 15–50 (1996).
64. Kresse, G. & Furthmüller, J. Efficient iterative schemes for ab initio total-energy calculations using a plane-wave basis set. *Phys. Rev. B* **54**, 11169–11186 (1996).
65. Blöchl, P. E. Projector augmented-wave method. *Phys. Rev. B* **50**, 17953–17979 (1994).

66. Sundararaman, R. et al. JDFTx: Software for joint density-functional theory. *SoftwareX* **6**, 278–284 (2017).
67. Sheppard, D., Xiao, P., Chemelewski, W., Johnson, D. D. & Henkelman, G. A generalized solid-state nudged elastic band method. *J. Chem. Phys.* **136**, 074103 (2012).
68. Henkelman, G., Uberuaga, B. P. & Jónsson, H. A climbing image nudged elastic band method for finding saddle points and minimum energy paths. *J. Chem. Phys.* **113**, 9901–9904 (2000).
69. Favaro, M. et al. Subsurface oxide plays a critical role in CO₂ activation by Cu (111) surfaces to form chemisorbed CO₂, the first step in reduction of CO₂. *Proc. Natl Acad. Sci. USA* **114**, 6706 (2017).
70. Ye, Y. et al. Dramatic differences in carbon dioxide adsorption and initial steps of reduction between silver and copper. *Nat. Commun.* **10**, 1875 (2019).

Acknowledgements

This project was supported by the Research Grant Council of Hong Kong SAR (Project numbers 16204818), NSFC-RGC Joint Research Scheme (N_HKUST607/17), the Innovation and Technology Commission (ITC-CNERC14SC01), the Guangzhou Science & Technology (Project 201704030134). This work was also supported by the Joint Center for Artificial Photosynthesis (JCAP), a DOE Energy Innovation Hub, supported through the Office of Science of the U.S. Department of Energy under Award No. DE-SC0004993. The calculations were performed on computer clusters at the materials and process simulation center (MSC) at Caltech, the high-performance computing (HPC) facility at Caltech, and the HKUST (funded by the School of Engineering).

Author contributions

M.D.H., W.A.G., and Z.T.L. conceived the idea and designed the research. M.D.H. performed all the calculations. M.D.H., Y.H., and T.H.Y. participated in discussions analyzing the data obtained from the calculations. M.D.H., W.A.G., and Z.T.L. wrote the paper with helpful comments from Y.H. and T.H.Y.

Competing interests

The authors declare no competing interests.

Additional information

Supplementary information is available for this paper at <https://doi.org/10.1038/s41467-020-16119-6>.

Correspondence and requests for materials should be addressed to W.A.G.I. or Z.L.

Peer review information *Nature Communications* thanks Alexis Bell, and other, anonymous, reviewer(s) for their contribution to the peer review of this work.

Reprints and permission information is available at <http://www.nature.com/reprints>

Publisher's note Springer Nature remains neutral with regard to jurisdictional claims in published maps and institutional affiliations.



Open Access This article is licensed under a Creative Commons Attribution 4.0 International License, which permits use, sharing, adaptation, distribution and reproduction in any medium or format, as long as you give appropriate credit to the original author(s) and the source, provide a link to the Creative Commons license, and indicate if changes were made. The images or other third party material in this article are included in the article's Creative Commons license, unless indicated otherwise in a credit line to the material. If material is not included in the article's Creative Commons license and your intended use is not permitted by statutory regulation or exceeds the permitted use, you will need to obtain permission directly from the copyright holder. To view a copy of this license, visit <http://creativecommons.org/licenses/by/4.0/>.

© The Author(s) 2020